Deformation of a Polydomain, Liquid Crystalline Epoxy-Based Thermoset

C. Ortiz,[†] R. Kim, E. Rodighiero, C. K. Ober,* and E. J. Kramer*,[‡]

Department of Materials Science and Engineering and The Materials Science Center, Bard Hall, Cornell University, Ithaca, New York 14850

Received September 30, 1997; Revised Manuscript Received March 25, 1998

ABSTRACT: Liquid crystalline thermosets (LCT's) were prepared by curing a difunctional LC epoxy monomer, diglycidyl ether of 4,4′-dihydroxy-α-methylstilbene, with the tetrafunctional cross-linker 4,4′-methylenedianiline (MDA). A commercial, non-LC epoxy monomer of similar starting molecular weight was also cured with MDA to produce an isotropic thermoset for comparison. Dynamic mechanical analysis revealed reduced glassy moduli, increased stiffness in the rubbery state, and broadened and lowered glass transitions for the LCT's compared to the isotropic thermoset based on the non-LC monomer. At room temperature, the true stress versus true strain curves of the LCT's under uniaxial compression showed no strain softening region, substantial plastic deformation ($\epsilon_f \approx 50\%$), and increased strain hardening compared to the isotropic thermoset. LCT's with a smectic type of local order exhibited bulk, homogeneous plastic yielding, which led to slow, stable crack propagation and an increased fracture toughness ($G_{Ic} = 1.62$ kJ/m^2, $K_{Ic} = 1.59$ MPa·m$^{1/2}$.

Introduction

It was de Gennes who first recognized in 1969 that "self-assembling" organized networks created by cross-linking rigid-rod, liquid crystalline molecules would have unique properties.[1] Subsequently, two new classes of materials emerged; densely cross-linked *liquid crystalline thermosets* (LCT's) and loosely cross-linked *liquid crystalline elastomers* (LCE's). Similar to conventional, isotropic, amorphous thermosets, LCT's are infusible, insoluble solids that have high glass transition temperatures ($T_g \approx 150$ °C) and high moduli ($E \approx 10^9$ Pa) at room temperature. In addition, the order of the liquid crystalline phase is "frozen" into the network; i.e., the material no longer exhibits liquid crystalline phase transitions even above T_g. LCE's have lower glass transition temperatures ($T_g < 35$ °C) and, hence, are rubbery at room temperature ($E \approx 10^6$ Pa). The high mobility of the network strands allows for large mechanical strains ($\epsilon_f \approx 200-300\%$), as well as reversible liquid crystalline phase transitions on heating and cooling. Recent experimental work on LCE's has revealed the existence of many remarkable phenomena, e.g., spontaneous shape changes at LC phase transitions,[2−4] strain-induced orientational transitions leading to new LC morphologies,[3−5] stress-induced macroscopic orientation,[6] and unique dynamic mechanical properties.[7−9] Warner et al.[10] have extended the theory of classical rubber elasticity to the case of LC networks and explained these effects as a result of the coupling between the entropy of the network, which tends to randomize its strands, and the enthalpic interaction between the rigid LC molecules, which tends to produce alignment along a preferred direction. This interaction is also present in densely cross-linked LCT's and poses a challenging theoretical problem that has yet to be explored fully.

LCT's (as well as liquid crystals in general) possess a unique heirarchical microstructure in that in the absence of external fields, they tend to form a macroscopically disordered *polydomain*, where each LC domain is defined as a region of uniform orientation. Locally, the molecules are oriented along a reference direction represented by a unit vector called the *director*, **n̂**. Most often, LCT's exhibit a fine-scaled field of wavy, dark brushes when viewed under the polarizing optical microscope, called a *Schlieren* texture (Figure 1). These brushes are visible where **n̂** is parallel or perpendicular to the polarizer or analyzer axes and emanate from orientational discontinuities in **n̂**, line defects called *disclinations*. Disclinations appear as points since the defect line is perpendicular to the page of the photograph. When the polarizer and analyzer are turned simultaneously in the crossed position, the disclination brushes move continuously across the area of the picture (rotating about the disclination points), indicating a continuous reorientation of **n̂**, while the disclination positions remain constant. Since the characteristic length scale of the texture (≈the mean distance between disclinations ≈ the LC domain size) is of the order of the wavelength of light (∼1 μm), the material appears opaque in bulk form.

A number of texts and reviews have been devoted to the theoretical and experimental treatment of the wide variety of LC textures and defects that have been observed.[11−20]

Within a single LC domain, the mesogens may exhibit one of a variety of liquid crystalline orderings. As shown in Figure 2, the molecules may be ordered locally into a *nematic* or *smectic* phase. The nematic phase has no positional order, while still maintaining long-range molecular orientational order (i.e., the molecules are constrained to orient themselves along **n̂**). The more ordered smectic phase exhibits parallelism of the molecular, long axis in addition to layering of the molecular centers of gravity in two-dimensional planes or sheets.

[†] Current address: Department of Polymer Chemistry, University of Groningen, Nijenborgh 4, 9747 AG Groningen, The Netherlands.

[‡] Current address: Departments of Materials and Chemical Engineering, University of California at Santa Barbara, Santa Barbara, California 93106-5050.

S0024-9297(97)01439-3 CCC: $15.00
Published on Web 06/05/1998

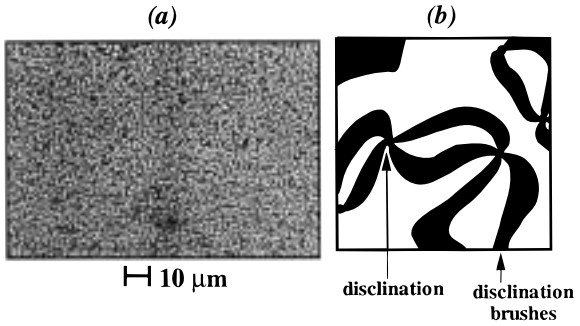

Figure 1. (a) Fine-scale, polydomain, Schlieren texture of DGDHMS/MDA thermosets as viewed under the polarizing optical microscope, (b) schematic of a large-scale, Schlieren texture (five disclinations are shown) as viewed under the polarizing optical microscope (ref 11 provided the micrograph used as the basis for this schematic).

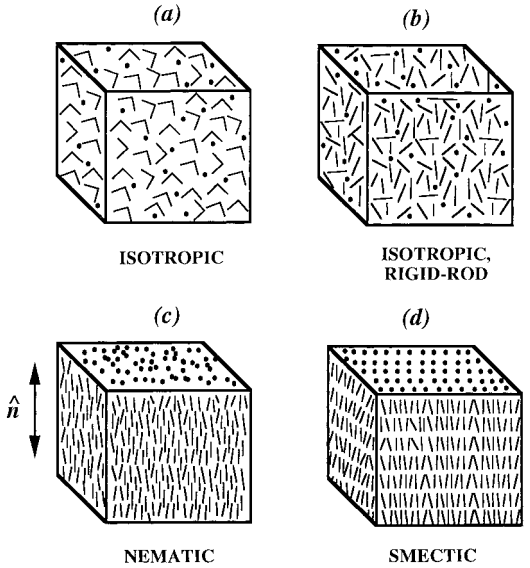

Figure 2. Schematics of local thermoset network structures (only monomers are depicted, cross-links are not shown): (a) isotropic network (made from non-LC monomer), (b) isotropic, rigid-rod network (made from LC monomer), (c) single LC domain in a nematic LCT, and (d) single LC domain in a smectic LCT.

An *isotropic, rigid-rod* network may be produced by carrying out the cross-linking in the isotropic phase and well above the clearing transition (i.e., the LC to isotropic phase transition) of the starting monomer. Isotropic thermosets based on non-LC monomers typically still retain much rigidity if the distance between cross-links is small.

LCT's have shown potential for improved thermal stability, orientational stability, low shrinkage upon cure, low coefficient of thermal expansion, low dielectric constant, and enhanced reaction rates due to the close proximity of the reactive groups. Although there have been relatively few reports on the mechanical properties of LCT's,[21−33] they have been dubbed "self-reinforcing" materials due to preliminary experiments that suggest improved impact resistance, fracture toughness, and stiffness above T_g. Most LCT's can be macroscopically oriented by curing in the presence of a strong electric or magnetic field and it is found that this orientation is thermally stable until degradation temperatures.[33] The prospect of well-controlled anisotropic electrical, optical, and mechanical properties has promoted research into their use as materials for structural applications (e.g., matrixes for composites), surface coatings, microelectronics packaging (e.g., high-temperature adhesives), and nonlinear optics. In addition, experiments on LCT's may provide insights on the anisotropic properties of oriented amorphous polymers produced by fabrication methods such as melt processing and injection molding.

Epoxies are one of the most important classes of thermosetting polymers that are widely used in a variety of industrial applications.[34−37] In this study, a stilbene-based LC diepoxide was chosen as a model system and cured with an aromatic, tetrafunctional diamine to produce densely cross-linked, polydomain LCT's with nematic and smectic types of local order. By curing at high temperatures within the isotropic phase of the epoxy/amine mixture, an isotropic, rigid-rod network could also be produced. An isotropic, epoxy-based network based on a commercial, non-LC monomer was also investigated and allowed for a direct comparison with experiments on the liquid crystalline and isotropic, rigid-rod networks.

Table 1. Chemical Structures and Thermal Transitions of Compounds Used in This Study[a]

Chemical Formulas	MW (g/mol)	Tm (°C)	T_{IN} (°C)	T_K (°C)
LC epoxy monomer,: diglycidyl ether of 4,4'-dihydroxy-α–methylstilbene (DGDHMS) 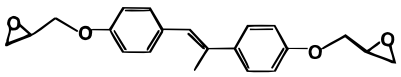	338	127	108	77
Non-LC epoxy monomer : diglycidyl ether of bisphenol A (DGEBA) 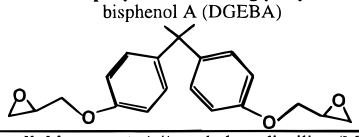	340	46	-	30
Crosslinking agent: 4,4'-methylene dianiline (MDA) 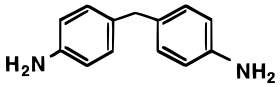	198	92	-	30
Stoichiometric mixture of DGDHMS / MDA	-	121	88-92	-
Stoichiometric mixture of DGEBA / MDA	-	60	-	-

[a] MW is the molecular weight, T_m is the melting point, T_{IN} is the isotropic-to-nematic transition temperature, and T_K is the crystallization temperature.

Experimental Section

Materials Analysis. The chemical structures and characteristics of the materials employed in this study are given in Table 1. The liquid crystalline epoxy monomer used in this study, diglycidyl ether of 4,4′-dihydroxy-α-methylstilbene (DGDHMS), was synthesized according to ref 38. Characterization was accomplished by thin-layer chromatography (TLC), Fourier transform infrared spectroscopy (Galaxy Series 2020 FTIR in KBr), and nuclear magnetic resonance (Varian XL-200 ^{1}H NMR**)**. A commerical, non-LC, epoxy monomer of similar molecular weight, diglycidyl ether of bisphenol A (DGEBA) was obtained from the Dow Chemical Co. (DER 332). The cross-linking agent, an aromatic tetrafunctional diamine, 4,4′-methylenedianiline (MDA), was obtained from the Aldrich Chemical Co. and used without further purification (purity >98%). Thermal transition temperatures of the monomers and each stoichiometric epoxy/amine mixture were characterized by differential scanning calorimetry (Dupont 2000 DSC cell, heating/cooling rate = 20 °C/min) and

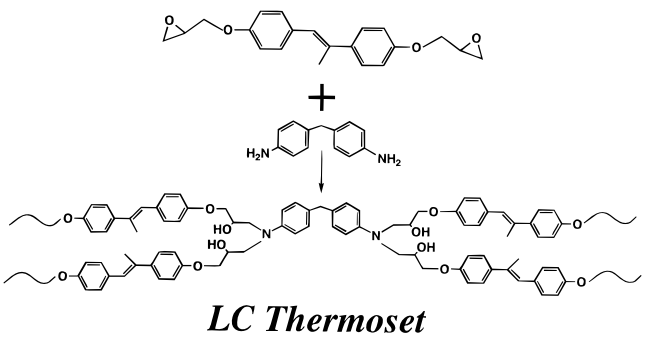

Figure 3. Cross-linking reaction of DGDHMS epoxy with 4,4′-methylenedianiline (MDA).

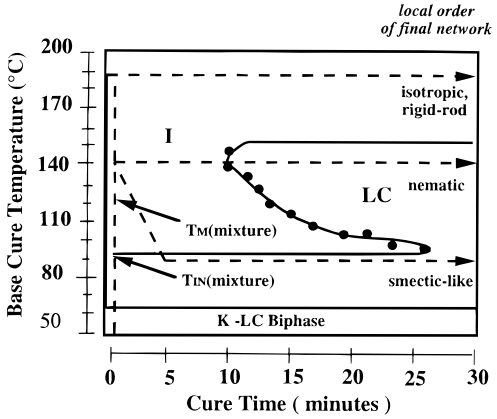

Figure 4. Isotropic−liquid crystalline time−temperature-transformation (TTT) diagram (—) and isothermal cure cycles (- - -) for the stoichiometric DGDHMS/MDA thermosetting system: "I" is the isotropic phase of the epoxy/amine mixture, "LC" is the liquid crystalline phase of the epoxy/amine mixture during cure, and "K" is the crystalline phase of the epoxy/amine mixture during cure.

polarizing optical microscopy, POM (Leitz, Inc.) in conjunction with a programmable hot stage (Mettler FP-82T, heating/cooling rate = 20 °C/min). The DGDHMS monomer is a monotropic nematogen, and the DGDHMS/MDA stoichiometric mixture exhibits a depressed isotropic-to-nematic transition temperature, T_{IN}, and very little crystallization at room temperature. The cross-linking reaction takes place as shown in Figure 3 and involves the reaction of primary and secondary amines with the glycidyl ether epoxy groups. Each hydrogen atom attached to a nitrogen atom opens up an epoxide ring and is converted into a secondary amine plus a secondary hydroxyl group. This secondary amine reacts with another epoxy group to form a tertiary amine and another secondary hydroxyl until complete cross-linking occurs.

Time−Temperature-Transformation (TTT) Diagram and Wide-Angle X-ray Diffraction (WAXD). To determine an appropriate set of cure cycles, the isotropic−liquid crystalline time−temperature-transformation (TTT) diagram was determined for isothermal cure cycles of the DGDHMS/MDA system using polarizing optical microscopy (Figure 4). The S-shaped curve represents the onset of the LC transformation as recorded by the appearance of strong birefringence and is seen to take place between 10 and 25 min cure time. The maximum cure temperature for obtaining a liquid crystalline network was approximately 150 °C. Lin and Yee et al.[39] have reported a similar TTT diagram for the curing of DGDHMS with the tetrafunctional, asymmetric diamine, sulfanilimide (SAA). Compared to MDA, the result was slower development of the LC phase (30−45 min cure time) and increased network stability with the maximum cure temperature for obtaining a LC network at approximately 190 °C. SAA is "reactively anisotropic"[40] (i.e., possesses amines of unequal reactivities) and should promote chain extension (by the more reactive groups) prior to cross-linking (by the less reactive groups) and, hence, earlier development of the LC phase. Since the opposite trend is observed, it is possible that MDA enhances the development of the LC phase through an increased reaction rate,[40] more extended chain conformations due to its symmetrical shape, or a combination of both these factors.

Because of the fine-grained nature of the LC textures of the final networks (Figure 1a), the distinction between nematic and smectic phases could not be determined solely by POM. To determine the type of local order present in the final cured networks, wide-angle X-ray diffraction (WAXD) was performed at the Cornell High Energy Synchotron Source (CHESS) on the DGDHMS/MDA thermosets cured isothermally at 180, 140, and 85 °C according to the procedure outlined in ref 40. For comparison, the DGEBA/MDA amorphous thermoset was also studied. The WAXD patterns displayed uniform rings, indicative of unoriented polydomain samples. For the DGDHMS/MDA thermosets the local network structure was found to be isotropic for 180 °C samples, nematic for the 140 °C samples, and smectic for the 85 °C samples with d spacings as follows: d = 4.8 Å (lateral packing of LC molecules), d = 13.4 Å (molecular long axis), and (for smectic samples) d = 22 Å (second-order reflection of smectic layer spacing), as shown in Figure 5. Hence, when curing was carried out starting from the nematic phase of the epoxy/amine mixture (i.e., at 85 °C); a transition took place to a more ordered smectic phase, which was then "locked into" the network. Curing at 140 °C from the isotropic phase of the epoxy/amine mixture also resulted in a more ordered network with a nematic local network structure. Curing far above T_{IN}(mixture) at 180 °C produced an isotropic, rigid-rod network. The smectic networks appeared opaque in bulk form with a high defect density, Schlieren texture (LC domain size ~1 μm) under the polarizing optical microscope. The nematic networks appeared translucent in bulk with a LC domain size approaching the resolution of the POM, producing a weakly birefringent uniform texture. The isotropic, rigid-rod DGDHMS/MDA networks and isotropic DGEBA/MDA networks were transparent and featureless under the POM. The isotropic DGEBA/MDA thermoset exhibited diffuse X-ray diffraction rings at d = 5.0 Å (lateral packing of the molecules) and d = 13.4 Å (molecular long axis), as shown in Figure 6.

Curing and Preparation of Bulk Samples. To prepare samples for mechanical testing, stoichiometric amounts of epoxy and amine were placed in molds constructed from glass slides and sealed with a silicone rubber sealant that was allowed to dry overnight. The glass slides had been previously soaked in a 3 mM solution of octadecyltrichlorosilane in 80/20 hexadecane/carbon tetrachloride to provide a nonreactive, nonstick coating. The mixtures were cured in a programmable oven according to the cure cycles outlined in Table 2. In general, the mixtures were first heated above their melting points. Second, they were quickly brought to the appropriate base cure temperatures (within ap-

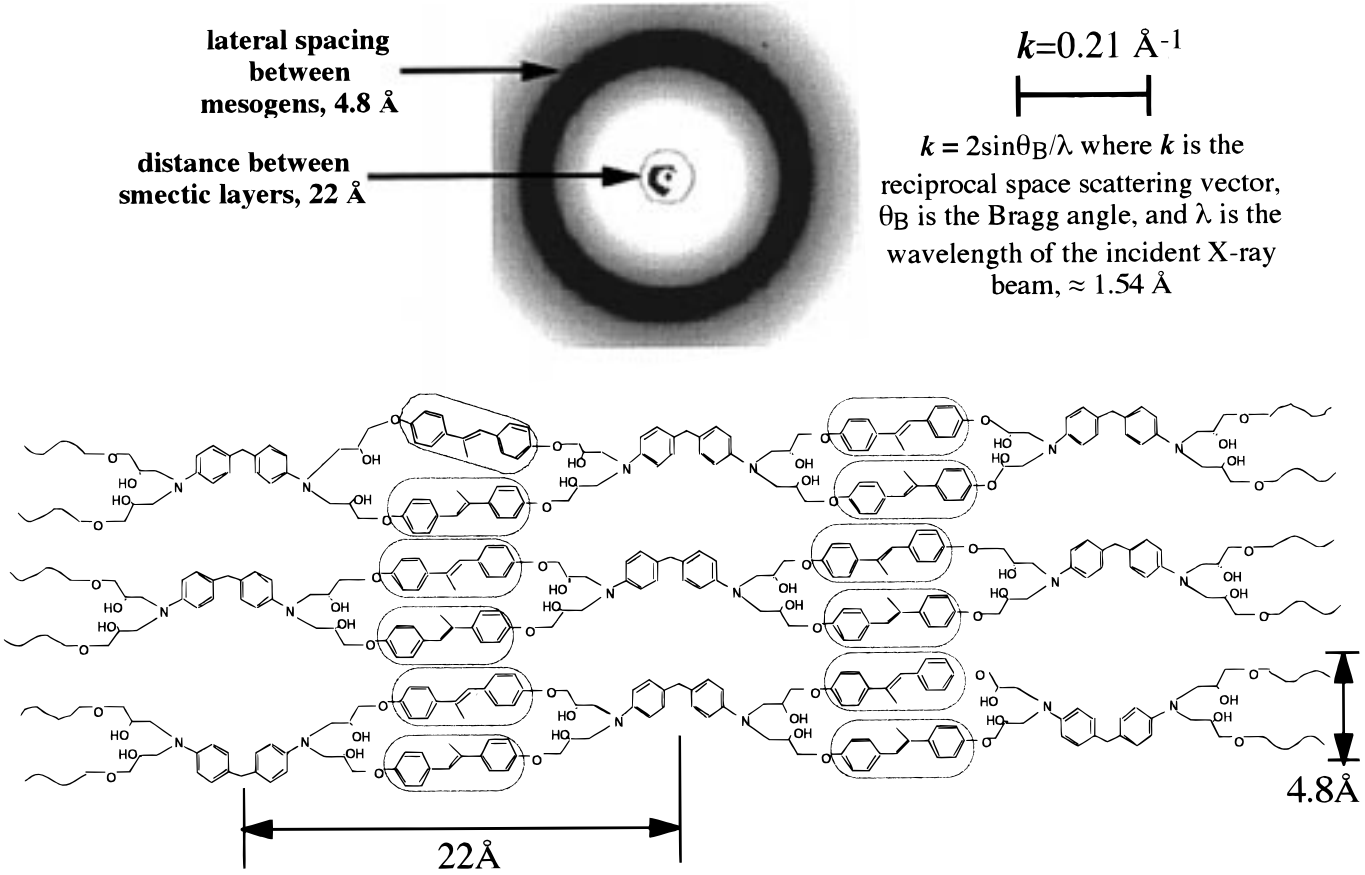

Figure 5. Wide-angle X-ray diffraction pattern of the DGDHMS/MDA smectic thermoset.

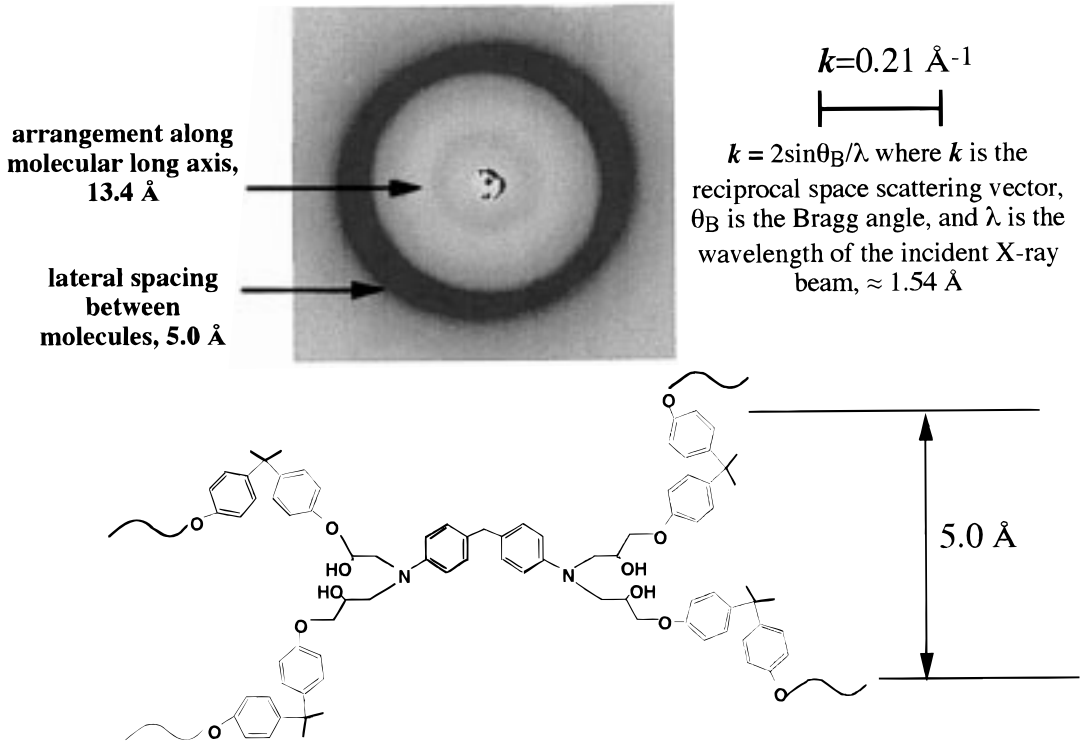

Figure 6. Wide-angle X-ray diffraction pattern of the DGEBA/MDA isotropic thermoset.

proximately 1 min) where they were held for 3 h. Postcure cycles at 180 °C for 2 h were then employed in order to devitrify the network and attain the maximum degree of cure.[41] After curing, the thermoset plaques were extracted from the molds and cut to the appropriate dimensions with a wafer-cutting machine and circular diamond saw blade (width = 0.04 in.). A reduction of the epoxide group concentration was verified for all samples by observing the infrared absorption peak at 918 cm^{-1} (Figure 7), which is due to the asymmetric stretch of the oxirane ring.[42] The extent of reaction, α, calculated from integration analysis of

Table 2. Three-Step Thermoset Cure Cycles

sample set	step 1: heat above T_m (epoxy/amine mixture) (°C)	step 2: bring to $T_{base\ cure}$ (°C) and hold 3 h	step 3: bring to $T_{postcure}$ (°C) and hold 2 h	phase at start of cure	phase at end of cure
DGDHMS/MDA	150	85	180	nematic	smectic
	150	140	180	isotropic	nematic
	180	180	180	isotropic	isotropic
DGEBA/MDA	180	180	180	isotropic	isotropic

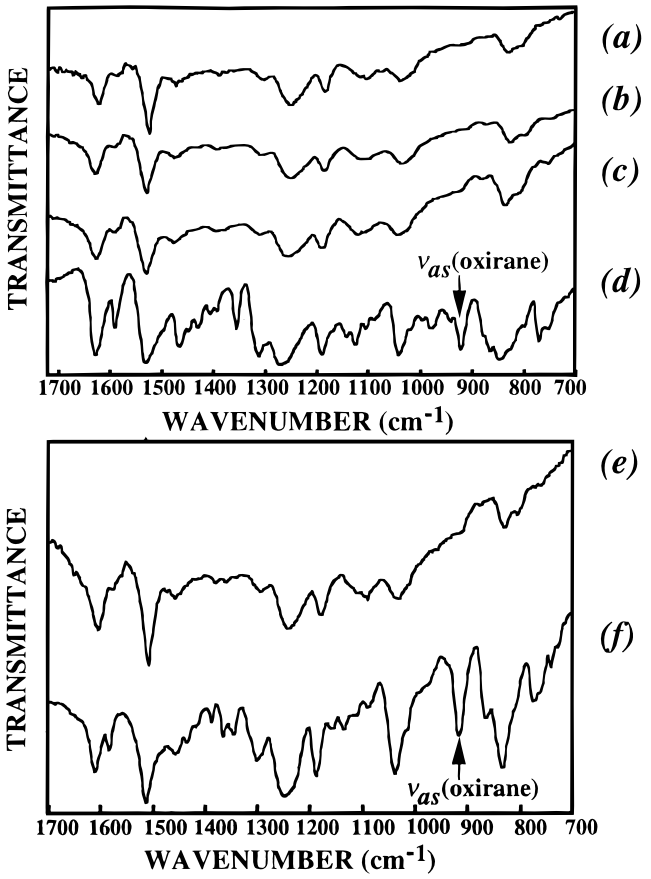

Figure 7. Fourier transform infrared (FTIR) spectra of epoxy monomers and cured thermosets (KBr): (a) DGDHMS/MDA smectic LCT, (b) DGDHMS/MDA nematic LCT, (c) DGDHMS/MDA isotropic, rigid-rod thermoset, (d) pure DGDHMS monomer, (e) DGEBA/MDA isotropic thermoset, and (f) pure DGEBA monomer.

the epoxy peak and normalized by the C=C benzene stretch (1512 cm^{-1}), was found to be between 99% and 100% for all samples. Soxhlet extractions were performed on the cured networks in methylene chloride for 24 h and produced extractables of ≈2−3 wt %.

Dynamic Mechanical Analysis, Uniaxial Compression, and Fracture Toughness Testing. The response of the network to small strain mechanical deformation was measured as a function of temperature using a Perkin-Elmer dynamic mechanical analyzer (DMA7) in a three-point bend configuration (Figure 8) with the span between supports equal to 15 mm and using a sphere probe of 3 mm diameter. The sample dimensions were 20 mm × 2 mm × 1 mm. The testing was carried out at a frequency, ω, of 1 Hz, a static stress of 1 MPa, a dynamic stress of 0.1 MPa, and a heating rate of 4 °C/min in a He atmosphere. Flexural storage moduli (E'), loss moduli (E''), and loss tangent (tan(δ)) were recorded as a function of temperature (20−300 °C) in stress-controlled mode. The glass-to-rubbery transition temperatures were recorded as the peak of the tan(δ) curve.

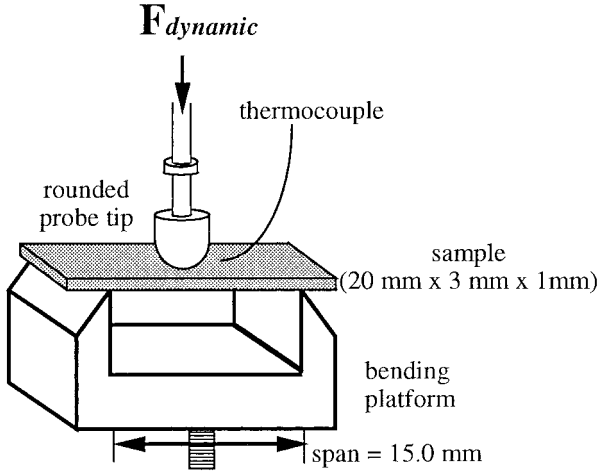

Figure 8. Experimental setup for dynamic mechanical analysis (DMA) of thermosets in three-point bend configuration.

Uniaxial compression was performed on 5.0 mm × 2.5 mm × 2.5 mm samples. The edges of each sample were polished flat manually with SiC 1200 grit sandpaper. Testing was done with an Instron (Model 1125) mechanical testing machine and a CCF compression load cell at a strain rate of 4.2×10^{-4} s^{-1}.

Plane strain fracture toughness experiments were conducted in accordance with ASTM E399-83 standards on 8 mm × 1.9 mm × 2.5 mm samples using a reduced-scale chevron notched three-point bend technique, as shown in Figure 9.[43,44] The application of this method for use with glassy polymers is relatively new and has a number of advantages. The geometry of the chevron notch typically promotes stable crack propagation and allows for the determination of the full force, P, versus displacement, δ, curve. The fracture toughness can then be evaluated from the area under this plot, instead of from the maximum load, P_{max}, as is done with other more conventional geometries. This reduces the large amount of inherent scatter in P_{max} due to the statistical nature of catastrophic fracture and allows for an averaging over the entire test. In addition, the samples are easy to machine, the testing does not need any specially designed devices, and bulk measurements can be made on materials that can only be obtained in small quantities.

The fracture toughness samples were first polished with 600-grit carbon polishing paper and subsequently with 5 μm diamond polishing paste and cloth using water as the lubricant. The chevron notch was produced with a 200 μm diameter wire cutter by making two orthogonal cuts at ±43° from the horizontal plane to produce an angle, θ, of 94°. Testing was carried out in displacement-controlled mode using an Instron Model 1125 mechanical testing machine, and automatic data acquisition of P (N) versus δ (μm) was achieved on a PC. Each beam was placed with the chevron notch facing up and directly above, but not touching, a linear variable differential transducer (LVDT), which was used

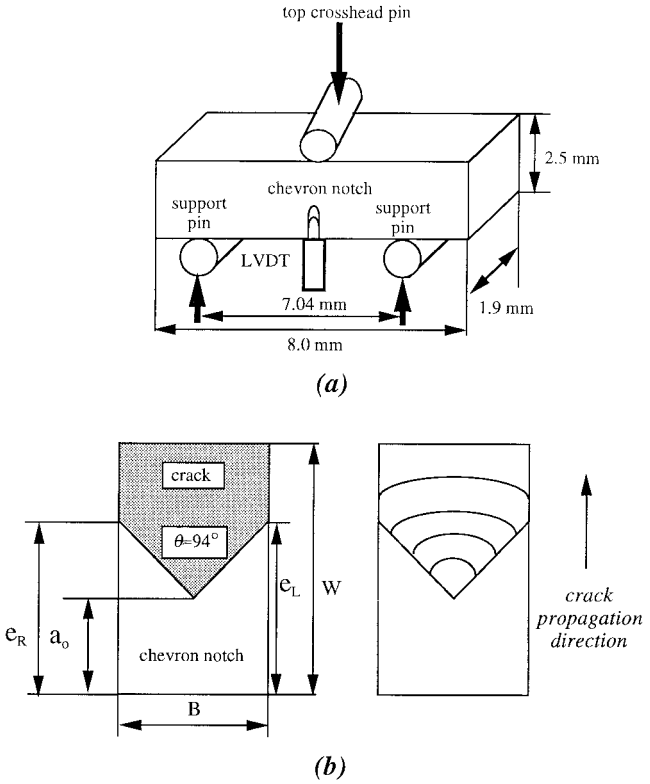

Figure 9. (a) Chevron-notched three-point bend technique for measuring fracture toughness of thermosets and (b) cross-sectional dimensions of fractured chevron-notched three-point bend thermoset samples.

to measure the displacement of the beam. The top crosshead pin was lowered onto the beam at a rate of 0.002 in./min until a small preload of approximately 0.75 N was achieved. The LVDT was then gently released so that it came into contact with the underside of the beam and the test was immediately started by lowering the top crosshead pin at a displacement rate of 0.002 in./min until the beam fractured. The cross-sectional dimensions, e_L, e_R, a_o, B, and W, of the fractured beams were then measured in millimeters by an optical microscope (Figure 9b).

Two measures of the plane strain fracture toughness, the critical strain energy release rate, G_{Ic} (kJ/m^2), and the critical stress intensity factor, K_{Ic} (MPa·m$^{1/2}$), were calculated using the following formulas:[45]

$$\mathrm{WOF} = U/2A \tag{1}$$

$$G_{Ic} = 2\mathrm{WOF} \tag{2}$$

$$K_{Ic} = G_{Ic}[E/(1-\nu^2)]^{1/2} \tag{3}$$

where WOF (kJ/m^2) is the work of fracture or effective energy required to separate the two surfaces, U (N·m) is the area under the F vs δ curve, A is the fracture area measured by optical microscopy (m^2), E is the elastic modulus (MPa) approximated by the small-strain dynamic mechanical glassy modulus at room temperature, and ν is Poisson's ratio (typically $\approx$0.32−0.44 for amorphous polymers[46]). This estimation assumes that the fracture toughness remains approximately constant with increasing crack length (i.e., a flat "R curve").

Failure analysis on the compression and fracture toughness samples was conducted using a JEOL 440 scanning electron microscope (SEM). The sample surfaces were coated with a Au−Pd alloy, and the sides of the samples were coated with copper paint to minimize charging.

Preparation of Sectioned Films from Bulk Samples. In some cases, the uniaxial compression tests were stopped just prior to failure in order to avoid fracture and maintain the sample in one piece. The compressed samples were then sectioned from bulk in the following manner.[47] Each side of the compressed sample was polished manually with 1200-grit SiC sanding paper, 6-, 1-, and 0.25-μm diamond polishing paste, and cloth until the sample surface appeared smooth and shiny. Films approximately 300 μm thick were cut in each of the three orthogonal directions parallel and perpendicular to the compression axis using a rotating diamond saw and *isocut* lubricant fluid. The films were washed with water to eliminate dust particles. A small drop of commercially available adhesive (i.e., Elmers "crazy glue") was deposited on a glass slide freshly cleaned with acetone. The tip of the polished side of the sample was placed face down on the glass slide and then slid into the end of the glue drop where it was held under pressure until it dried. Hence, a portion of the sample that was not attached to the glass slide could be removed after polishing with a sharp razor blade for subsequent experiments. The bottom of the glass slide was attached with double-sided tape to an aluminum sample mount typically used for polishing metallographic samples. The entire assembly was then flipped over and polished manually with 1200-grit SiC sandpaper until the film thickness was approximately 20−50 μm. The sample was then finished by polishing with 6-, 1-, and 0.25-μm diamond polishing pastes and cloth.

Birefringence Measurements and WAXD on Compressed Thermosets. A uniaxial liquid crystal has two principal refractive indices, n_o and n_e. The first, n_o, is observed for an "ordinary" ray associated with a light wave where the electric vector vibrates perpendicular to the optic axis. The "extraordinary" index, n_e, is observed for a linearly polarized light wave where the electric vector is parallel to the optic axis. In the case of nematic or smectic liquid crystals, the optical axis is given by the director, $\hat{\mathbf{n}}$. Using the subscripts $\parallel$ and $\perp$ to denote directions parallel and perpendicular to $\hat{\mathbf{n}}$, then

$$n_o = n_\perp$$

$$n_e = n_\parallel \tag{4}$$

$$\Delta n = n_\parallel - n_\perp = n_o - n_e$$

The absolute value of the birefringence, $|\Delta n|$, was measured using the compensation technique[48] on a Zeiss Jenapol polarizing optical microscope in monochromatic light with $\lambda = 578$ nm. In this method, the birefringent LC sample is placed between crossed polars with its slow and extraordinary axis, i.e., along the director, $\hat{\mathbf{n}}$, in the 45° position (Δn = maximum). A compensator (i.e., a material with adjustable birefringence) is then inserted with its slow axis at 135° between the sample and the analyzer so that $\hat{\mathbf{n}}$ is perpendicular to the compensator axis. The adjustable optical path difference (OPD) of the compensator and the liquid crystal

add up, giving the total retardation:

$$\mathrm{OPD}_{\mathrm{total}} = \mathrm{OPD}_{\mathrm{compensator}} + [n(135°) - n(45°)]t \quad (5)$$

where t is the thickness of birefringent material. The OPD of the compensator is then changed until complete extinction occurs and $\mathrm{OPD}_{\mathrm{total}} = 0$, giving

$$|\Delta n|_{\mathrm{sample}} = \frac{\mathrm{OPD}_{\mathrm{compensator}}}{\text{sample thickness}} \quad (6)$$

If $\hat{\mathbf{n}}$ is parallel to the compensator axis, the optical path differences of the liquid crystal and the compensator will not be able to cancel and extinction will not occur. Instead, the birefringent interference colors will move successively up the Michel−Levy color chart.[47] Typically, there is a linear relationship between Δn and the degree of macroscopic orientation (i.e., the degree to which the individual LC domains, represented by local LC directors, $\hat{\mathbf{n}}$, are aligned with respect to an externally applied field), as characterized by the orientation parameter, S:

$$\Delta n = \Delta n_{\mathrm{max}} S \quad (7)$$

$$S = \frac{3\langle \cos^2 \varphi \rangle - 1}{2} \quad (8)$$

where φ is the angle between the LC domain directors, $\hat{\mathbf{n}}$, and the externally applied field, $\langle\ \rangle$ denotes an average of $\cos^2 \varphi$ over all possible LC domains, and Δn_{max} is the "intrinsic" birefringence for a perfectly aligned sample ($\mathbf{S} = 1$). Δn_{max} is highly dependent on chemical structure, but a typical value for a monodomain liquid crystal is 0.2.[49] $|\Delta n|$ was measured in the three orthogonal directions parallel and perpendicular to the compression axis.

Wide-angle X-ray diffraction patterns were taken of the compressed, oriented thermosets at CHESS parallel and perpendicular to the compression axis according to the procedure described previously.

Results and Discussion

Dynamic Mechanical Analysis. Figure 10 and Table 3 compare the dynamic mechanical properties of the thermosets employed in this study. With regard to rubbery deformation ($T > T_g$), one of the most notable results is the extremely high values of the rubbery moduli for the LCT's, especially with the increasing degree of local order (i.e., the smectic networks). This phenomenon was also observed for oriented epoxide LCT's,[24] as well as epoxide thermosets containing biphenol structures,[50] and will be discussed further relative to the classical theory of rubber elasticity.[51]

For Gaussian networks, classical rubber elasticity predicts a tensile rubbery modulus as follows:

$$E_{\mathrm{R}} \approx 3G_{\mathrm{R}} = \frac{3\rho RT}{\langle M_x \rangle} = 3\nu_x k_{\mathrm{B}} T \quad (9)$$

where G_{R} is the rubbery shear modulus, ρ is the density of the network, T is the absolute temperature, R is the universal gas constant, k_{B} is Boltzmann's constant, ν_x is the network strand density, and $\langle M_x \rangle$ is the average molecular weight between cross-links based on stoichiometry. For densely cross-linked networks, the assumptions of classical rubber elasticity are highly questionable, if not completely invalid. Non-Gaussian behavior is expected when network strands are extended so that the end-to-end distance $\langle r^2 \rangle^{1/2}$ exceeds 30−50% of its fully extended length.[51] LeMay and Kelley[52] find that a DGEBA epoxy molecule of MW 360, with about nine flexible main chain bonds, is already extended about 33% of its fully extended length even before cross-linking. Hence, it is not truly Gaussian. To assess the possibility of using classical rubber elasticity theory to describe the behavior of non-LC thermosets above T_g, a plot of E_{R} versus $\langle M_x \rangle$ was constructed, as shown in Figure 11. Here we compare experimental data on epoxies cured with both aliphatic and aromatic amines,[52−56] the data of this study, and the prediction of classical rubber elasticity theory as represented by eq 9. Surprisingly, it is seen that the classical theory describes the observed experimental trend reasonably for the DGEBA-based isotropic thermosets above T_g.

This result is in agreement with the work of King and Andrews,[57] who showed that stress/strain data of cured epoxy resins above T_g can be fitted to a straight line in a Mooney−Rivlin plot of $\sigma_n/2(\lambda - \lambda^{-2}) = C_1 + C_2\lambda^{-1}$ versus λ^{-1}, where σ_n is the nominal stress in a uniaxial tension test, λ is the extension ratio in a uniaxial tension test, C_1 is the intercept of the Mooney-Rivlin plot and

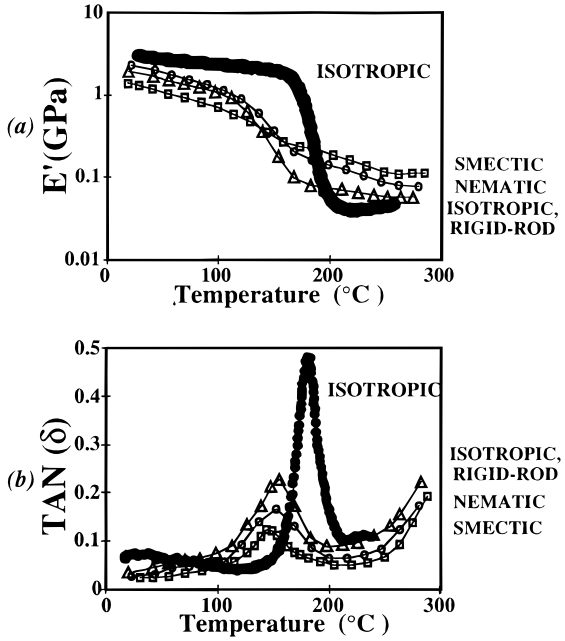

Figure 10. (a) Dynamic storage moduli, E', and (b) dynamic loss tangent, tan(δ), as a function of temperature for the DGDHMS/MDA and DGEBA/MDA thermosets: smectic (□), nematic (○), and isotropic, rigid-rod (△), compared to the isotropic DGEBA/MDA thermoset (●).

Table 3. Summary of Dynamic Mechanical Data of Networks Used in This Study[a]

material	network structure	E'_{RT} (GPa)	E'_{R} (MPa)	T_α (°C)
DGDHMS/MDA	smectic	1.34	115	147.2
DGDHMS/MDA	nematic	2.42	80	153.5
DGDHMS/MDA	isotropic, rigid-rod	2.03	59	158.1
DGEBA/MDA	isotropic	3.14	53	181.8

[a] E'_{RT} is the glassy storage modulus measured at room temperature, E'_{R} is the storage modulus at the rubbery plateau (i.e., measured at 275 °C), and T_α is the glass-to-rubbery transition temperature as measured by the peak of the tan(δ) versus temperature plot.

Reference	System (Epoxy/Crosslinker)
Bell et al.[53]	△ DGEBA / MDA, isotropic
Glad et al.[54]	○ DGEBA / MDA, isotropic
Lemay et al.[52]	□ DGEBA / DDS, isotropic
Katz et al.[55]	× DGEBA / EDA, isotropic
	DGEBA / DETA, isotropic
	DGEBA / TETA, isotropic
	DGEBA / TEPA, isotropic
	DGEBA / MBCA, isotropic
Kaelble [56]	+ DGEBA / $H_2NC_{36}H_{63}NH_2$, isotropic
This study	▣ DGEBA / MDA, isotropic
This study	◇ DGDHMS / MDA : smectic LCT
	○ DGDHMS / MDA : nematic LCT
	△ DGDHMS / MDA : isotropic, rigid-rod

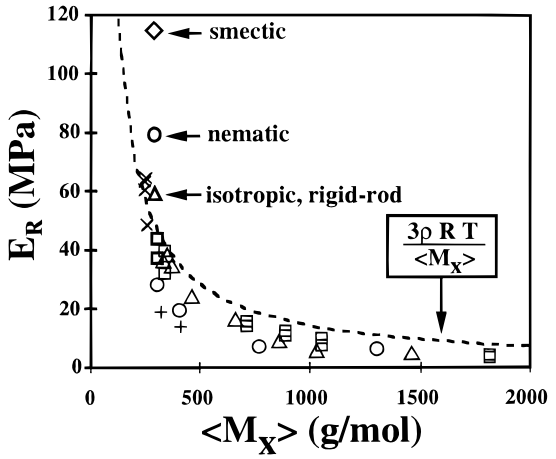

Figure 11. Plot of the rubbery plateau modulus, E_R (MPa), versus molecular weight between cross-links based on stoichiometry, $\langle M_x \rangle$ in order to compare experimental data with the prediction of classical rubber elasticity theory, i.e., eq 9 (- - -); the cross-linker abbreviations are as follows: MDA is 4,4′-methylenedianiline, EDA is ethylenediamine, DDS is 4,4′-diaminodiphenyl sulfone, DETA is diethylethylenetriamine, TETA is triethylene tetramine, TEPA is triethylene pentamine, and MBCA is methylene bis(*o*-chloroaniline).

equal to $\rho RT/2\langle M_x \rangle$, and C_2 is the slope of the Mooney−Rivlin plot. Surprisingly, even traditional elastomers such as polyisoprene,[58] poly(dimethylsiloxane),[59] and natural rubber[60] deviate greatly from the straight line prediction of rubber elasticity in a Mooney−Rivlin plot.

For materials such as the LCT's, however, classical rubber elasticity severely underestimates the experimental values of the rubber moduli. The "finite extensibility" of the rigid LC molecules may lead to enthalpic deformations that perturb or overshadow the entropic response of the network. This effect is commonly observed in isotropic, amorphous networks at high strains, resulting in a dramatic increase in stress at large strains, "strain hardening", and will be described in some detail later on. The deformation of rigid-rod, "enthalpic" networks (i.e., containing localized cross-link sites) and rigid-rod, "entropic" networks (i.e., containing freely hinged cross-link sites) has been considered theoretically by Boué et al.,[61] Vilgis,[62] and Jones and Marques[63] using energetic arguments. Their formulation results in an increase in E_R, which is controlled by the thermal fluctuations of the rigid, LC mesogens. Terentjev[64] asserts that thermal fluctuations in such networks are extremely small, if not negligible, due to the elastic free energy penalty for distortions in the director field. Experimental evidence cited[65] is the fact that monodomain (highly oriented) nematic elastomers are highly transparent and do not scatter light as

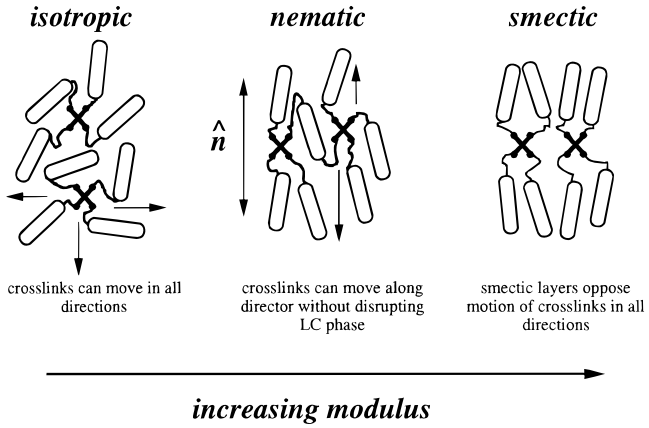

Figure 12. Schematic showing possible molecular explanation for increased rubbery modulus in LCT's above T_g.

equivalent turbid, monodomain nematic fluids.

Figure 12 illustrates a simplistic molecular explanation for the trend of increased rubbery moduli with increasing degree of local order for the thermosets based on the LC monomer. In these networks, it is plausible to assume that the deformation will be dominated by the entropic response and mobility of the ring-opened epoxy groups and MDA cross-link sites. When a stress is applied to an isotropic, rigid-rod network, the cross-links are free to move in all directions without disrupting the local structure of the network. In the nematic phase, however, the cross-link motion is restricted in the direction perpendicular to the director and would result in a free energy penalty for disruption of the LC phase. In the smectic phase, the cross-links are restricted in an additional direction, parallel to the director or along the smectic layers, thus resulting in the highest modulus. The decreasing value of the modulus with increasing temperature above T_g, peculiar to LCT's, could then be attributed to a reduction in degree of local order.

When the LCT's were deformed in the glassy state ($T < T_g$), they displayed lowered moduli, broadened and lowered glass transitions, and a decreased tan(δ) peak height compared to the isotropic network based on the non-LC monomer. These trends become more pronounced in the LC systems with decreasing $T_{\text{base cure}}$, i.e., as they are cured deeper into the LC phase. The broadened tan(δ) peak is an indication of an increase in the breadth of the distribution of relaxation times of macromolecular chain motions as the sample goes through the glass transition. However, it is hard to interpret these data conclusively since glassy deformations are primarily governed by intermolecular van der Waals forces and short-range enthalpic deformations of the individual molecules, e.g., bending, rotating, and stretching of network strands.[66] Surprisingly, such deformations may be facilitated by the planar molecular structure of the LC mesogen and, instead, may possibly be due to density effects.

Uniaxial Compression (Isotropic Thermoset). Since densely cross-linked, isotropic thermosets are relatively brittle materials, it is impossible to deform thick specimens in uniaxial tension without fracture intervening at relatively small strains, usually before the onset of macroscopic ductility. Hence, mechanical tests are usually conducted in uniaxial compression in order to obtain significant postyield flow. Figure 13a is a plot of true stress, σ_t, versus true strain, ϵ_t, for the

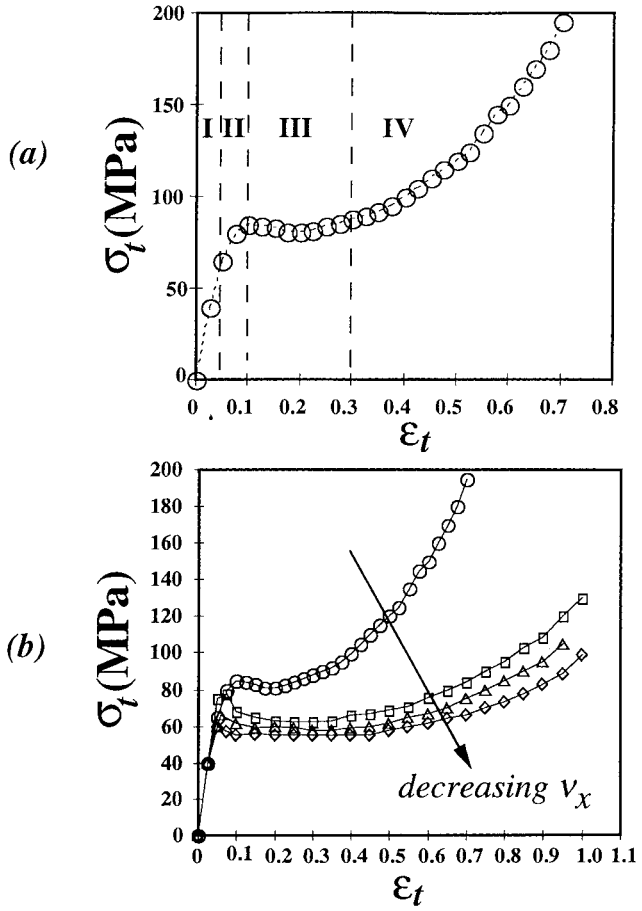

Figure 13. True stress versus true strain curve for amorphous, epoxy-based thermosets of stoichiometric DGEBA/MDA in uniaxial compression; the starting molecular weights, M_R, were (a) 350 (○) and (b) (compared with the data of Glad[54]) 1050 (□), 1850 (△), and 3600 (◇).

isotropic DGEBA/MDA thermoset in uniaxial compression. As for most amorphous glassy polymers, one can distinguish four distinct regions: (I) linear viscoelastic, i.e., glassy deformation, (II) homogeneous yielding, i.e., plastic deformation, (III) strain softening, and (IV) strain hardening. Figure 13b compares our data with the data of Glad[54] for the same DGEBA/MDA system with increasing starting molecular weight of the epoxy resin, M_R: 1050, 1850, and 3600. These experiments show a decrease in the amount of strain hardening and an increase in strain softening with decreasing network strand density.

The nature of each of these regions is described in detail elsewhere[68−70] and will be summarized here for a direct comparison with the LCT's. As described in the previous section, short-range, glassy deformations occur at small strains (region I) and involve bending, stretching, and small angular rotations of the network strands. With increasing stress, the chains are able to overcome an intermolecular resistance to rotation and shear and begin to give homogeneous yield (region II). Subsequently, "strain softening" ensues where the flow stress decreases with increasing strain (region III). This instability is common to most glassy polymers and results in inhomogeneous yielding, which can often lead directly to ductile failure. It is thought that strain softening results from shear-induced changes in the structure of the glass.[70] The more compliant strain-softened regions are subject to larger local strains and strain rates than the unyielded portions, frequently

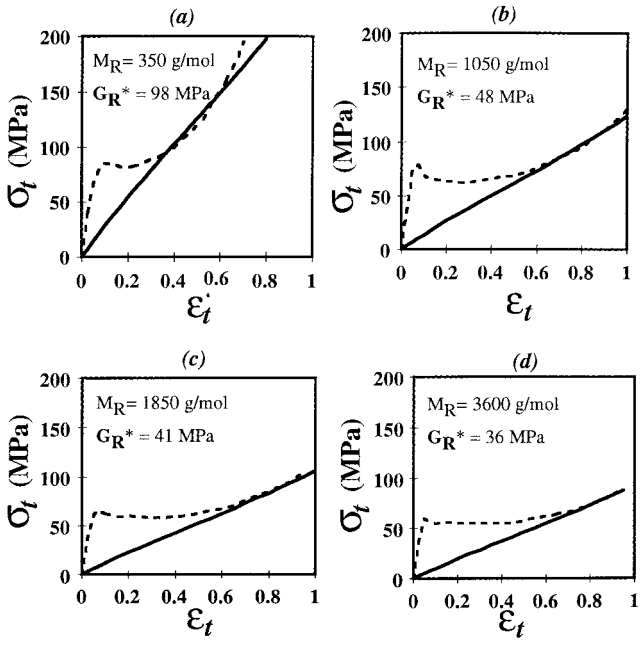

Figure 14. Determination of shear "modulus," G_R^*, by fitting the classical rubber elasticity equations to the strain-hardening region of DGEBA/MDA amorphous, non-LC thermosets in uniaxial compression.

resulting in microshear bands and shear patches. At high enough strains, the network strands undergo large-scale changes in chain conformation and begin to orient parallel to the tensile stretch direction or perpendicular to the compression axis, thus producing a macroscopically anisotropic material. As a result of this phenomenon, it is thought that an entropic "back stress" produces a dramatic increase in σ_t in region IV of the flow curve. Strain hardening is necessary to stabilize the softened regions of plastic instability since without it those regions that yielded first would continue to deform to failure.

Attempts to model the strain-hardening region of glassy polymers using rubber elasticity theories have met with limited success for polycarbonate and poly(methyl methacrylate).[71,72] Figure 14 illustrates the use of this approach to predict a tensile "modulus," $E_R^* \approx 3G_R^*$ (for an isotropic material, $E = 2G(1 + \nu)$ where ν = Poisson's ratio), by fitting the strain hardening region of the stress versus strain curve of the DGEBA/MDA amorphous thermoset with the rubber elasticity formula for uniaxial deformation:[51]

$$\sigma_t = G_R(\lambda^2 - 1/\lambda) \tag{9}$$

where λ is equal to $\exp(\epsilon_t)$. The results are compared with experimental data in Figure 15. The rubber elasticity prediction captures the decreasing trend with increasing molecular weight between cross-links but there is a large overestimation of E_R, suggesting that although this deformation involves large-scale changes in chain conformation, it is still very different than that above T_g.

A microscopic model has been proposed by Krupenkin[73] to predict and explain the origins of strain softening and strain hardening in amorphous polymer glasses. A freely jointed polymer chain consisting of "beads and springs" embedded in a polymer matrix is considered. The equations of motion are derived both analytically and numerically by assuming that each bead has a

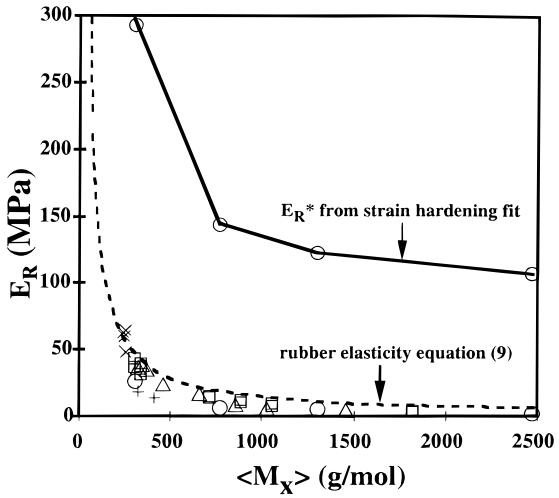

Figure 15. Evaluation of the use of classical rubber elasticity theory to fit the strain-hardening regime of non-LC, amorphous DGEBA/MDA thermosets in uniaxial compression.[54]

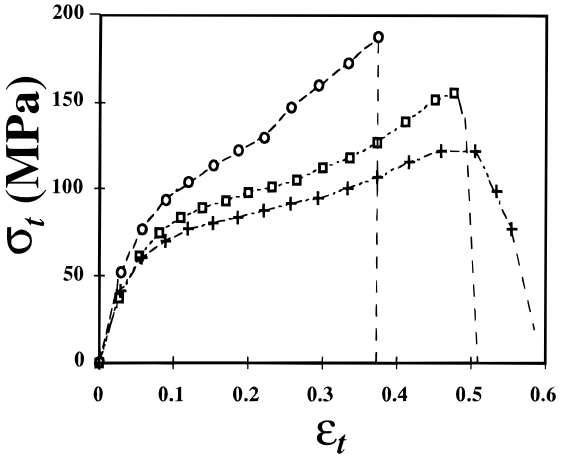

Figure 16. True stress versus true strain curves for DGDHMS/MDA thermosets deformed in uniaxial compression: smectic LCT (+), nematic LCT (□), and isotropic, rigid-rod thermoset (○).

friction coefficient and a force/velocity law. A force is applied to the ends of the chain and the mobility along the chain is derived, thus allowing for the prediction of mechanical properties (e.g., stress versus strain curves).

The extensive plastic deformation and macroscopic anisotropy that isotropic networks experience in uniaxial compression is stable at room temperature for extended periods of time, essentially "locked in" by the glassy phase. Upon heating, the DGEBA/MDA network retains a complete memory of the original cross-linked configurations and exhibits a 100% recovery of the plastic strain well below T_g (≈90 °C).

LC and Isotropic, Rigid-Rod Thermosets. The uniaxial compression data for the LCT's and isotropic, rigid-rod thermosets are given in Figure 16 and summarized in Table 4. Compared to the isotropic DGEBA/MDA thermoset, the flow curves of the LCT's exhibit a lower yield stress, similar compressive modulus ($E \approx 2$ GPa), no strain-softening region, and reduced fracture strain, ϵ_f. The reduction in ϵ_f observed for the LCT's compared to the isotropic thermoset may be a result of the polymer chains between cross-links being highly extended, as expected for such rigid molecules. As the samples are cured deeper into the LC phase, the material becomes more ductile and exhibits a reduced

Table 4. Compression Data of Networks Used in This Study[a]

material	network structure	σ_Y (MPa)	ϵ_Y	σ_f (Mpa)	ϵ_f
DGDHMS/MDA	smectic-like	38	0.028	110	0.51
DGDHMS/MDA	nematic	38	0.028	148	0.49
DGDHMS/MDA	isotropic rigid-rod	51	0.030	175	0.37
DGEBA/MDA	isotropic	50	0.05	205	0.75

[a] σ_Y is the 0.02% offset yield stress, ϵ_Y is the yield strain, σ_f is the fracture strength, and σ_f is the fracture strain.

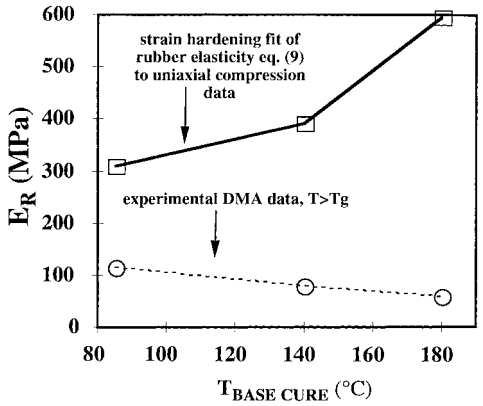

Figure 17. Evaluation of the use of classical rubber elasticity theory to fit the strain hardening region of liquid crystalline DGDHMS/MDA thermosets in uniaxial compression.

amount of strain hardening. This trend is exactly opposite to that observed for the small strain rubbery deformation (i.e., the smectic phase exhibited the highest modulus, E_R). The absence of the strain-softening region suggests that the network strands are so extended that they are unable to deform by localized plastic zones. However, instead of the quick brittle fracture of polymer chains, the LCT's deform by homogeneous, bulk plastic deformation. The moduli predicted from eq 9 are compared with experimental data in Figure 17, and here one can see that not only is there an overestimation of E_R but the trend is exactly the opposite. The LCT's and isotropic, rigid-rod thermoset also exhibited 100% recovery of strain when heated well below T_g (≈90 °C).

The macroscopic failure modes of the thermosets used in this study are drawn schematically in Figure 18a. The isotropic DGEBA-based network and isotropic, rigid-rod DGDHMS-based network exhibit sudden, catastrophic failure (characterized by a single, distinct σ_f) by fracture into numerous smaller pieces of various sizes and shapes, leading to a macroscopically rough fracture surface with "frayed" edges, as observed by eye. Failure is initiated along planes inclined at 45° to the compression axis (i.e., the direction of maximum shear stress, τ_{max}). For the nematic and smectic LCT's, failure typically takes place in two steps. First, a major crack appears at 45° to the compression axis and propagates relatively slowly for some time until sudden catastrophic failure occurs with the appearance of two or three more large cracks located on other planes also oriented at 45° to the compression axis. A macroscopically fibrillar or grooved fracture surface is seen by inspection of the failed samples. Scanning electron micrographs shown in Figure 18b display deep, curved ridges as well as voids. The smectic LCT's exhibit increased ductility and usually a single stable, slowly propagating crack can be observed tearing at 45° to the compression direction.

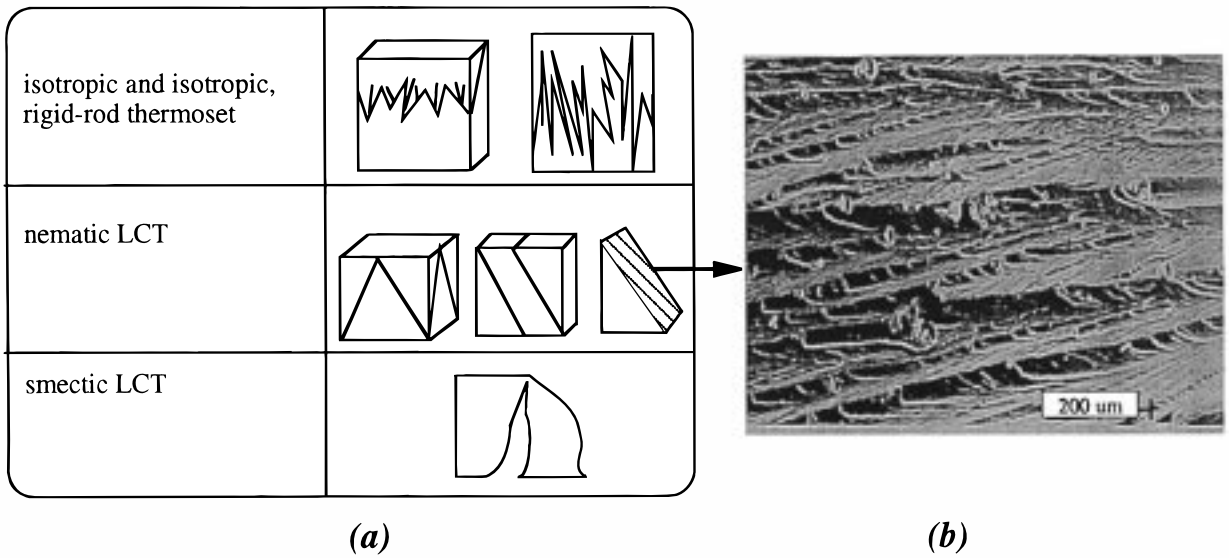

Figure 18. (a) Schematics of macroscopic compression failure modes of thermosets and (b) compressive fracture surfaces typical of polydomain nematic and smectic LCT's as viewed under the scanning electron microscope.

Table 5. Birefringence, $|\Delta n|$, of Compressed, Sectioned Thermosets

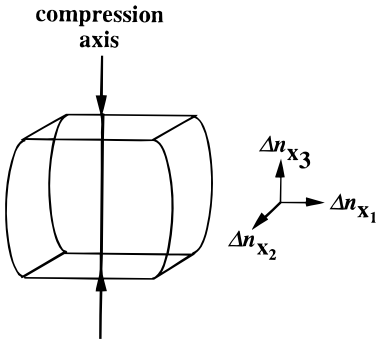

material	x_3	x_1	x_2
DGEBA/MDA, amorphous	0.005	0.045	0.048
DGDHMS/MDA, isotropic	0.004	0.039	0.049
DGDHMS/MDA, nematic	0.004	0.042	0.040
DGDHMS/MDA, smectic	0.008	0.020	0.024

The failed smectic samples typically remained in one piece.

Birefringence Measurements and WAXD on Compressed Thermosets. The birefringence measurements are summarized in Table 5 and indicate that all of the samples were macroscopically oriented by the mechanical stress, similar to liquid crystalline elastomers.[6] In all cases, $\Delta n_{x1,x2} \gg \Delta n_{x3}$ with the maximum birefringence achieved at failure, $\Delta n_{x1,x2} \approx 0.045$ (for nematic, isotropic, rigid-rod, and isotropic) and $\Delta n_{x1,x2} \approx 0.022$ (smectic). These results indicate a preferred molecular orientation for $\hat{\mathbf{n}}$ to lie perpendicular to the compression axis and random within this plane, i.e., a planar orientation distribution and negative orientation parameter S (Figure 19). Even though the planar state is uniaxially oriented, it is one of rather low orientation, since S is determined by the component of $\hat{\mathbf{n}}$ along the x_1 and x_2 axis. The oriented samples were observed to possess many disclinations when viewed under the polarizing optical microscope. WAXD was employed (Figure 20) to further confirm the planar orientation of the molecules. It was found that the local smectic order was conserved during mechanical orientation (as indicated by the small-angle reflections at ~22 Å).

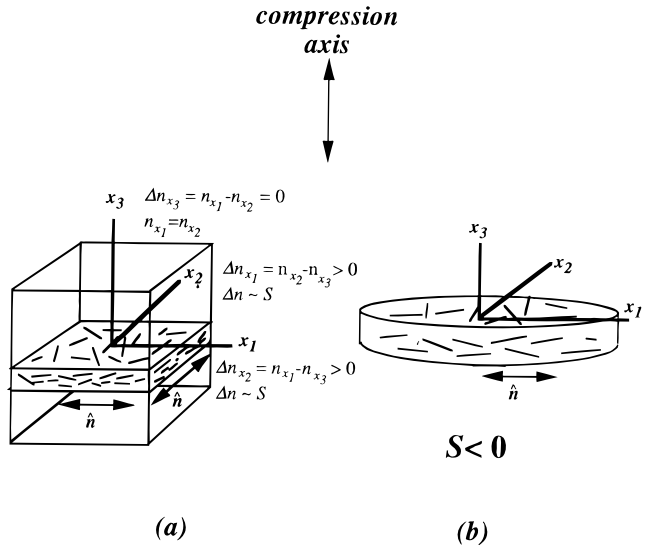

Figure 19. Deformation of uniaxially compressed thermosets: (a) macroscopic planar orientation and (b) corresponding orientation distribution function.

Fracture Toughness. The shape of the load versus displacement curve in a mechanical test (shown schematically in Figure 21) can be associated with macroscopic failure mechanisms and divided into a variety of categories;[54,69,74,75] (a) brittle, unstable, (b) brittle, stable, (c) initially brittle with "stick-slip," (d) initially brittle with complex fracture, (e) semibrittle, (f) semiductile, (g) ductile, and (h) ductile with complex fracture. Combinations of these modes are also possible. The load (N) versus displacement (μm) curves for the three-point bend, chevron-notched fracture toughness experiments in this study are given in Figure 22a−d. The load magnitudes should not be compared in these plots since the original sample and chevron-notch dimensions are different. The resulting calculations of G_{Ic} and K_{Ic} from these curves for the DGDHMS/MDA thermosets are given in Table 6. The fracture toughness calculation for the DGEBA/MDA isotropic thermoset is not reported here since fracture occurred before the entire load versus displacement curve could be obtained. Figure

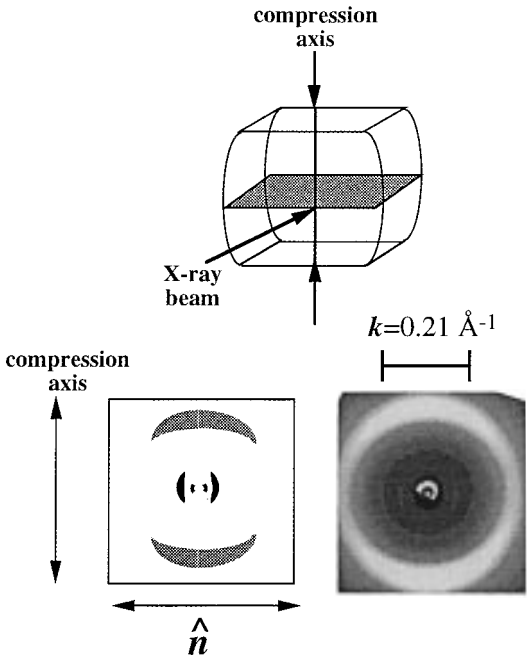

Figure 20. Schematic and WAXD pattern of compressed, oriented DGDHMS/MDA smectic thermoset where $k = 2 \sin \theta_B/\lambda$ where k is the reciprocal space scattering vector, θ_B is the Bragg angle, and λ is the wavelength of the incident X-ray beam, ≈1.54 Å.

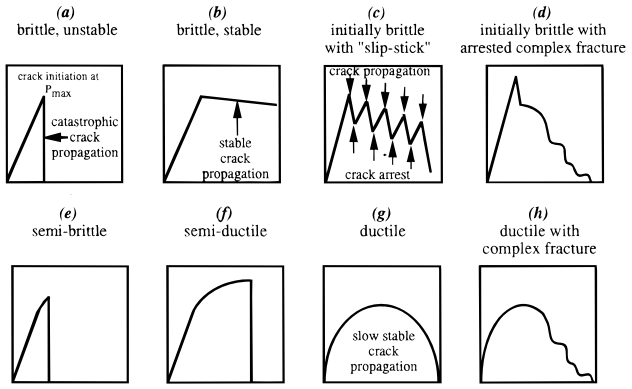

Figure 21. Schematics of typical load versus displacement curves and corresponding fracture mechanisms for different types of materials.[54,69,77,78]

23 shows scanning electron micrographs of the fracture surfaces of the failed samples.

Isotropic Thermoset. The fracture of amorphous, isotropic thermosets based on non-LC epoxy monomers has been studied extensively.[52,54,66,69,70,75−79] Although these materials may exhibit large-scale macroscopic plastic deformation in uniaxial compression, their tensile deformation, for example, at crack tips, is much more localized and typically leads to catastrophic, brittle fracture. Even in the chevron-notched, three-point bend fracture toughness test (the geometry of which promotes stable crack propagation), the DGEBA/MDA thermoset exhibits a linear load versus displacement curve (Figure 22a) up to a maximum load, at which time a crack is initiated and propagates catastrophically in a brittle manner across the sample. The fracture surface appears smooth and featureless under the SEM (Figure 23a), a typical characteristic of brittle fracture. If epoxy networks were truly brittle, they would have a theoretical fracture toughness of at most, $G_{Ic} = 1.0$ J/m^2, due to main chain bond scission that is necessary for formation

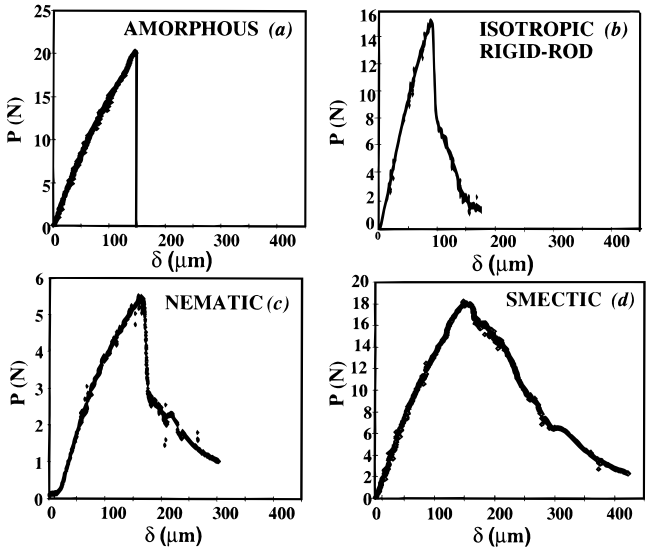

Figure 22. Typical load, P, versus displacement, δ, curves for thermosets in the chevron-notched three-point bend fracture toughness tests: (a) DGEBA/MDA isotropic thermoset, (b) DGDHMS/MDA isotropic, rigid-rod thermoset, (c) DGDHMS/MDA nematic LCT, and (d) DGDHMS/MDA smectic LCT.

Table 6. Estimates of the Plane Strain Fracture Toughness for the Thermosets Measured by the Chevron-Notched Three-Point Bend Fracture Toughness Test[a]

thermoset	G_{Ic} (kJ/m^2)	K_{Ic} (MPa·m$^{1/2}$)
DGDHMS/MDA, smectic	1.62	1.59
DGDHMS/MDA, nematic	0.75	1.46
DGDHMS/MDA, isotropic, rigid-rod	0.68	1.27
DGEBA/MDA, isotropic (typical value, refs 70−73	0.40	1.21

[a] The critical strain energy release rate, G_{Ic} (kJ/m^2), and critical stress intensity factor, K_{Ic} (MPa·m$^{1/2}$), calculated from eqs 2 and 3, respectively (using $\nu \approx 0.38$).

of the cleavage surface.[76] Measured values of G_{Ic}, however, are typically of the order of 100−400 J/m^2.[77−79] The additional energy required to propagate the crack has been shown by Glad[54] to be expended in the formation of a small, diffuse plastic zone (∼8 μm in width) immediately ahead of the crack tip. This shear deformation zone contains network strands that possess a preferred orientation along the tensile axis and are strained to approximately 20% greater than the surrounding film.

Since G_{Ic} values of 100−400 J/m^2 are still relatively low, many other methods of toughening epoxy thermosets and other amorphous, glassy polymers have been investigated intensely in recent years,[80−92] including (1) chemical modification (e.g., using more flexible backbone structures or curing agents), (2) promotion of localized or bulk shear yielding (e.g., by decreasing the network strand density through increasing the starting monomer molecular weight or using low-functionality curing agents), (3) promotion of crazing, (4) second and multiphase toughening (e.g., fillers such as rubber particles, block copolymers, immiscible polymers, fibers, thermoplastics, etc.), and (5) macroporous, void-filled thermosets. One of the most effective and common techniques, producing up to an order-of-magnitude toughness improvement, is to use a fine dispersion of phase-separated rubber particles in a glassy polymeric matrix.[83−90] It is thought that the main toughening mechanism of

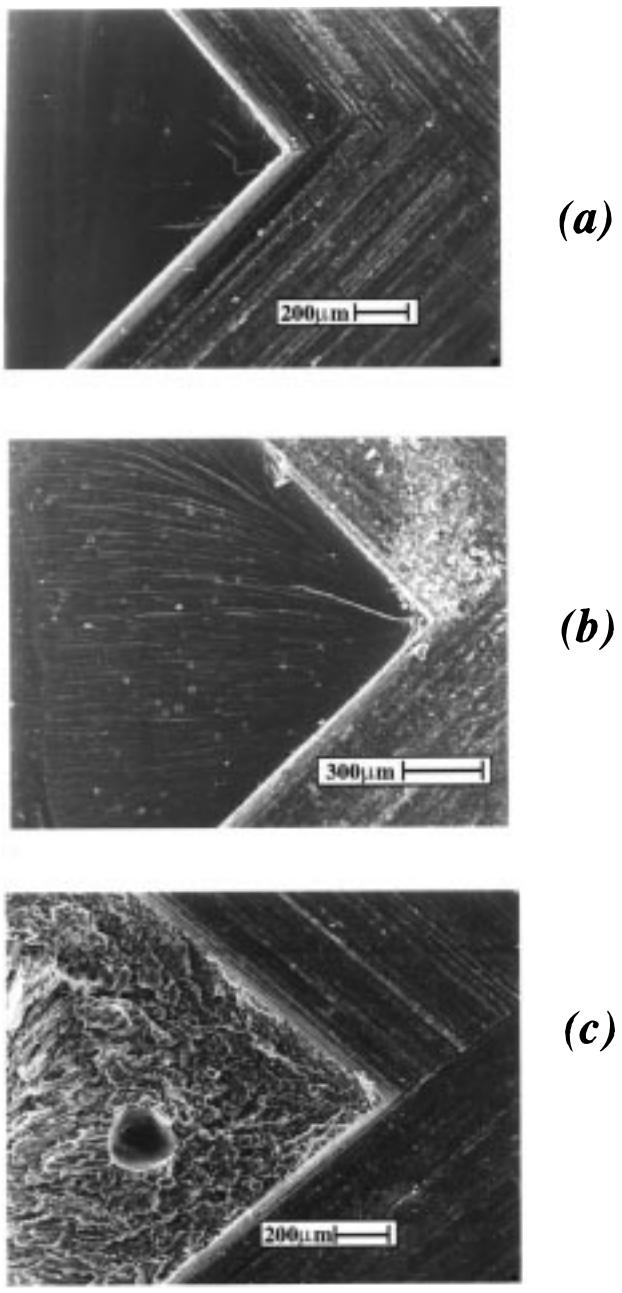

Figure 23. Scanning electron micrographs (SEM) of cross-sectional surfaces of thermosets fractured in the chevron-notched three-point bend technique: (a) DGEBA/MDA isotropic thermoset, (b) DGDHMS/MDA nematic LCT, and (c) DGDHMS/MDA smectic LCT.

these materials comes from rubber particles that cavitate under stress, thus generating a series of voids that can relieve triaxial stresses in the matrix and promote the energy-absorbing process of shear yielding.[91,92] Macroporous, void-filled thermosets have been produced via chemically induced phase separation[81] by employing nonreactive, low molecular weight, low boiling point liquids that phase separate during the curing process and can be subsequently evaporated by heating the network above T_g. Crazing[82] is another effective toughening process in loosely cross-linked ($\nu_x < 4 \times 10^{25}$ strands/m^3) and un-cross-linked polymers. In this case, a localized, irreversible volume expansion occurs through the formation of void-filled, highly strained, fibrillar, cracklike structures called "crazes", which can sustain loads between the crack faces. In general, glassy

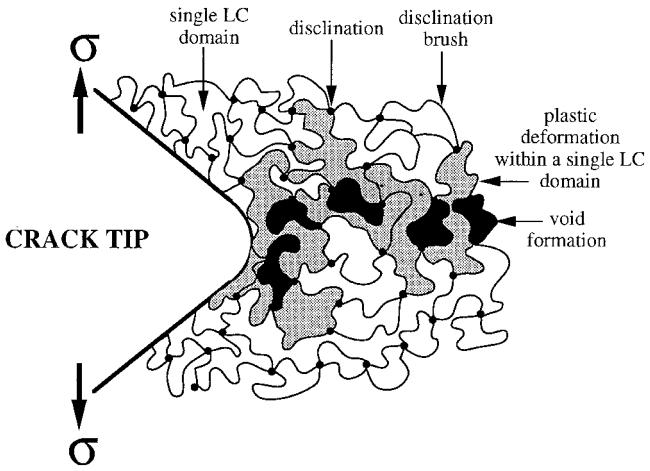

Figure 24. Schematic of proposed fracture mechanism in a polydomain smectic liquid crystalline thermoset.

polymers will be toughened by any micromechanism that promotes energy absorption such as noncatastrophic microcrack initiation, crack branching (changes in the crack propagation direction), crack pinning (stopping of crack propagation), and crack bridging (material spanning across the crack surfaces behind the crack tip, thus inhibiting crack propagation).

LC and Isotropic, Rigid-Rod Thermosets. The DGDHMS/MDA isotropic, rigid-rod and nematic thermosets exhibit stable crack propagation, which takes place in two steps (Figure 22b,c) similar to type (d) in Figure 21d). First, they exhibit a regime of relatively fast crack propagation followed by more nonuniform crack propagation at slower speeds (as indicated by the reduced slope and nonlinearity of the P versus δ curve at high displacements). A cross-sectional SEM (Figure 23b) of the fracture surfaces shows that the isotropic, rigid-rod and nematic DGDHMS/MDA samples exhibited parabolic, elongated deformation markings, indicative of some limited plastic deformation. The DGDHMS/MDA smectic LCT exhibits only slow, stable crack propagation for the duration of the experiment, similar to their behavior in uniaxial compression (Figure 22d, similar to type (h) in Figure 21h) and indicative of complex, ductile fracture. A cross-sectional SEM (Figure 23c) of the fracture surface shows that the smectic DGDHMS/MDA thermosets exhibited voiding and an extremely rough and highly deformed fracture surface, suggesting that bulk plastic deformation had occurred. Overall, there is a general increase in fracture toughness with decreasing $t_{\text{base cure}}$, i.e., when the local order is increased from isotropic and nematic to smectic. The smectic phase exhibited the highest fracture toughness with values of $G_{Ic} = 1.62$ kJ/m^2 and $K_{Ic} = 1.59$ MPa·m$^{1/2}$.

Proposed Toughening Mechanism of Smectic LCT's. The proposed fracture mechanism responsible for the high fracture toughness of the smectic LCT's is shown schematically in Figure 24. As the network is deformed, it is difficult to maintain the continuity of the polydomain microstructure (especially with such a high cross-link density) and, instead, it is likely that the LC domains prefer to fail in an individual and isolated manner. The network strands of unfavorably oriented domains (perpendicular or nearly perpendicular to the stress direction) should be "softer"[93] and fail first, thus producing microscopic voids and defects ahead of the crack tip. Neighboring domains can then deform under uniaxial rather than triaxial stress and undergo sig-

nificant plastic deformation, similar to rubber-modified thermosets. There is some evidence for this process from recent work on LCT thin films strained in tension and investigated under the polarizing optical microscope[94] and transmission electron microscope.[21] This type of fracture is similar to noncatastrophic microcrack formation in polycrystalline metals, which also results in extensive plastic deformation.[95] The stable crack propagation observed in the smectic LCT's most likely takes place through the slow growth and interconnecting of these voids, leading to the macroscopically fibrillar fracture surfaces observed under the SEM. Most likely, we do not observe as much plastic deformation in the nematic LCT's because the domain size is too small to generate voids of a large enough size.

Conclusions

The mechanical properties of thermosets based on a liquid crystalline epoxy monomer have been investigated and compared to an isotropic thermoset based on a non-LC monomer of similar starting molecular weight. Many differences were observed as a function of the local degree of order in the LC-based networks as well as between the LC and non-LC based systems.

Dynamic Mechanical Analysis. It was found that the LCT's exhibited increased stiffness in the rubbery state ($T > T_g$), reduced glassy moduli ($T < T_g$), and broadened and lowered glass transitions compared to the isotropic thermoset based on the non-LC monomer. The trend in E_R versus $\langle M_x \rangle$ for the isotropic, non-LC based thermoset could be well described by the theory of classical rubber elasticity, even at very high cross-link densities (~1 monomer between cross-link sites). E_R of the LCT's, especially that of the smectic phase, greatly exceeded that of the amorphous thermoset and, hence, also the prediction of classical rubber elasticity, possibly due to the restricted motion of the cross-links within the ordered LC phase.

Uniaxial Compression. The LCT's exhibited unique stress/strain curves with a lower yield stress compared to the amorphous thermoset and lack of strain softening, indicative of homogeneous plastic deformation. Fitting the strain-hardening region of uniaxial compression stress versus strain data to the classical rubber elasticity equation, $\sigma_t = G_R(\lambda^2 - 1/\lambda)$, led to the correct trend in E_R versus $\langle M_x \rangle$ for the isotropic, non-LC based thermoset, but also a large overestimation in the numerical values. Hence, strain hardening cannot be solely due to an entropic back stress. Taking this approach for the LCT's resulted in the wrong trend, as well as inaccurate numerical values. All of the thermosets studied could be macroscopically oriented in uniaxial compression and recovered their original network structure and dimensions upon heating well below the glass transition ($T \approx 90$ °C).

Fracture Toughness. The isotropic, non-LC based thermoset exhibited catastrophic, brittle failure and very low fracture toughness. The smectic LCT's exhibited the highest fracture toughness values ($G_{Ic} = 1.62$ kJ/m^2 and $K_{Ic} = 1.59$ MPa·m$^{1/2}$) and slow, stable, crack propagation due to bulk, homogeneous plastic yielding. It is thought that the high toughness of the smectic phase results from the isolated fracture of individual domains, thus producing microscopic defects and voids near and around the crack tip. The triaxial stresses in neighboring domains are relieved by this process, thus enabling substantial plastic deformation.

Acknowledgment. The authors would like to acknowledge the following people who assisted in polymer synthesis: Jia Shiun-Lin, Audrey Robinson, Dr. Yakhov Freidzon, Dr. Allen Gabor, Dr. Scott Clingman, Dr. Guo Ping Mao, and Dr. Hilmar Koerner. For technical consultation we would also like to to thank Dr. Hilmar Koerner, Atsushi Shiota, and Maura Weathers (X-ray diffraction experiments and analysis), Margaret Rich (optical microscopy), John Hunt (SEM), and George Chevalier (mechanical testing). This research was sponsored by the National Consortium for Graduate Degrees for Minorites in Science and Engineering (GEM, Inc.), the Department of Education (DOE), and the National Science Foundation (NSF).

References and Notes

(1) de Gennes, P. G. *Phys. Lett.* **1969**, *A28*, 725.
(2) Brehmer, M.; Zentel, R. *Mol. Cryst. Liq. Cryst.* **1994**, *243*, 353.
(3) Mitchell, G. R.; Davis, F. J.; Guo, W. *Phys. Rev. Lett.* **1993**, *71*, 2047.
(4) Küpfer, J.; Finkelmann, H. *Makromol. Chem. Rapid Commun.* **1991**, *12*, 717.
(5) Kundler, I.; Finkelmann, H. *Macromol. Chem. Rapid. Commun.* **1995**, *16*, 679−686.
(6) Schätzle, J.; Kaufhold, W.; Finkelmann, H. *Makromol. Chem.* **1989**, *190*, 3269−3284.
(7) Pakula, T.; Zentel, R. *Makromol. Chem.* **1991**, *192*, 2401.
(8) Gallani, J. L.; Hilliou, L.; Martinoty, P.; Doublet, F.; Mauzac, M. *J. Phys. II Fr.* **1996**, *6*, 443−452.
(9) Deeg, F. W.; Diercksen, K.; Schwalb, G.; Brauchle, C.; Reinecke, H. *Phys. Rev. B* **1991**, *44* (6), 2830.
(10) Warner, M.; Terentjev, E. M. *Prog. Polym. Sci.* **1996**, *21*, 853−891.
(11) Demus D.; Richter L. *Textures of Liquid Crystals*; VCH Publications: Deerfield Beach, FL, 1978.
(12) Kléman, M. In *Liquid Crystals and Plastic Crystals*; Gray, G. W., Winsor, P. A., Eds.; Ellis Horwood Ltd.: Chichester, England, 1974; Vol. 1, p 75.
(13) Kléman, M. *Advances in Liquid Crystals*; Academic Press: New York, San Francisco, London, 1975; Vol. 1, p 267.
(14) Bouligand, Y. *Defects and Textures in Liquid Crystals: Dislocations in Solids*; Nabarro, F. R. N., Ed.; North-Holland: Amsterdam, 1980; Vol. 5, Chapter 23.
(15) Gray, G. W. *The Microscope* **1976**, *24*, 117.
(16) Hartshorne, N. H.; Stuart, A. *Crystals and the Polarizing Microscope*, 4th ed.; Arnold: London, 1970.
(17) Hartshorne, N. H. *The Microscopy of Liquid Crystals*; Microscope Publications: Ltd.: London, Chicago, 1974.
(18) Hartshorne, N. H. In *Liquid Crystals and Plastic Crystals*; Gray, G. W., Winsor, P. A., Eds.; Ellis Horwood Ltd.: Chichester, England, 1974; Vol. 2, p 24.
(19) Saupe, A. In *Liquid Crystals and Plastic Crystals*; Gray, G. W., Winsor, P. A., Eds.; Ellis Horwood Ltd.: Chichester, England, 1974; Vol. 2, p 28.
(20) Hudson, S., Ph.D. Thesis, University of Massachusettes, 1990.
(21) Sue, H.-J.; Earls, J. D.; Hefner, R. E., Jr. *Deformation, Yield, and Fracture of Polymers: Proceedings of the 10th Annual International Conference of the Institute of Materials*; Churchill College, Cambridge, U.K., April 7−10th, 1997; Chameleon Press Ltd: 1997; pp 129−132.
(22) Laus, M.; Pernozzoli, R.; Koerner, H.; Ober, C. K. XII convegno italiano di scienza e tecnologia delle macromolecole, Palermo, Italy, 1995; pp 661−664.
(23) Earls, J. D.; Hefner, R. E., Jr. European Patent Appl. 0−379−057A2, assigned to the Dow Chemical Co., 1990.
(24) Jahromi, S.; Kuipers, W. A. G.; Norder, B.; Mijs, W. J. *Macromolecules* **1995**, *28*, 2201−2211.
(25) Hikmet, R. A. M.; Broer, D. J. *Polymer* **1991**, *32* (9), 1627−1632.
(26) Carfagna, C.; Amendola, E.; Giamberini, M. *Composite Struct.* **1994**, *27*, 37−43.
(27) Carfagna, C.; Amendola, E.; Giamberini, M. In *Liquid Crystalline Polymers: Proceedings of the International Workshop on Liquid Crystalline Polymers*, Capri, Italy, June 1−4, 1993; Carfagna, C., Ed.; Pergamon Press: Oxford, U.K., 1994; pp 69−85.
(28) Su, W.-F. A. *J. Polym. Sci., Part A: Polym. Chem.* **1993**, *31*, 3251−3256.

(29) Shiota, A.; Ober, C. K. *J. Polym. Sci., Phys. Ed.* **1998**, *36*, 31−38.
(30) Litt, M. H.; Whang, W.-T.; Yen, K.-T.; Qian, X.-J. *J. Polym. Sci., Part A: Polym. Chem.* **1993**, *31*, 183−191.
(31) Melissaris, A. P.; Litt, M. H. *Macromolecules* **1994**, *27*, 2675−2684.
(32) Melissaris, A. P.; Sutter, J. K.; Litt, M. H.; Scheiman, D. H.; Scheiman, M. *Macromolecules* **1995**, *28*, 860−865.
(33) Barclay, G. G.; McNamee, S. G.; Ober, C. K.; Papathomas, K. I.; Wang, D. W. *J. Polym. Sci., Part A: Polym. Chem.* **1992**, *30*, 1843−1853.
(34) Lee, H.; Neville, K. *Handbook of Epoxy Resins*; McGraw-Hill: New York, 1967.
(35) Ellis, B. *Chemistry and Technology of Epoxy Resins*; Blackie Academic and Professional: London, 1993.
(36) May, C. A.; Tanaka, G. Y. *Epoxy Resin Chemistry and Technology;* Marcell Dekker: New York, 1973.
(37) Bauer, R. S. *Epoxy Resin Chemistry*; Advances in Chemistry 114; American Chemical Society: Washington, DC, 1979.
(38) Barclay, G. G.; McNamee, S. G.; Ober, C. K.; Papathomas, K. I.; Wang, D. W. *J. Polym. Sci., Part A: Polym. Chem.* **1992**, *30*, 1831−1843.
(39) Lin, Q.; Yee, A. F.; Earls, J. D.; Hefner, R. E., Jr.; Sue, H.-J. *Polymer* **1994**, *35*, 2679.
(40) Shiota, A.; Ober, C. K. *Polymer*, in press. (SAA is expected to be much less reactive than other aromatic amine compounds, as electrons on the nitrogen atom in the amine function are strongly withdrawn by the sulfone function. The reduced reactivity of SAA is supported by electron density calculations reported in this reference.)
(41) Wisanrakkit, G.; Gillham, J. K. *J. Appl. Polym. Sci.* **1990**, *41*, 2885−2929.
(42) Pavia, D. L.; Lamptnan, G. K.; Kriz, G. K., Jr. *Introduction to Spectroscopy: A Guide for Students of Organic Chemistry*; W. B. Saunders: Philadelphia, 1979; p 46.
(43) Wu, S.-X. In *Chevron-Notched Specimens: Testing and Stress Analysis*; ASTM STP 855; Underwood, J. H., Freiman, S. W., Baratta, F. I., Eds.; American Society for Testing Materials: Philadelphia, 1984; pp 176−192.
(44) Jenkins, M. G.; Ferber, M. K.; Ghosh, A.; Peussa, J. T.; Salem, J. A. *Chevron-Notch Fracture Test Experience: Metals and Non-Metals*; ASTM STP 1172; Brown, K. R., Baratta, F. I., Eds.; American Society for Testing Materials: Philadelphia, 1992; pp 159−177.
(45) Munz, D. *Fract. Mech. Ceram.* **1983**, *6*, 1−26.
(46) Seitz, J. T. *J. Appl. Polym. Sci.* **1993**, *49*, 1331. For the K_{Ic} calculations ν was assumed to be ≈0.38.
(47) Helmsley, D. A. *Applied Polymer Light Microscopy*; Elsevier Applied Science: New York, 1979; Chapter 1.
(48) Gay, P. *An Introduction to Crystal Optics*; Longman, Inc.: New York, 1967; Chapter 9, pp 107−154.
(49) Brunet-Germain, C. R. *Hebd. Sean. Acad. Sci.* **1970**, *B271*, 1075.
(50) Shiraishi, T.; Motobe, H.; Ochi, M.; Nakanishi, Y.; Konishi, I. *Polymer* **1991**, *33* (14), 2975−2980.
(51) Treloar, L. R. G. *The Physics of Rubber Elasticity*; Claredon Press: Oxford, U.K., 1975.
(52) LeMay, J. D.; Kelley, F. N. *Adv. Polym. Sci.* **1986**, 115−147.
(53) Murayama, T.; Bell, J. P. *J. Polym. Sci.* **1970**, *A28*, 437.
(54) Glad, M. D. Ph.D. Thesis, Department of Materials Science and Engineering, Cornell University, Ithaca, NY, 1990.
(55) Katz, D.; Tobolsky, A. V. *Polymer* **1963**, *4*, 417.
(56) Kaeble, D. H. *J. Appl. Polym. Sci.* **1965**, *9*, 1213−1225.
(57) King, N. E.; Andrews, E. H. *J. Mater. Sci.* **1978**, *13*, 1291−1302.
(58) Kawabata, S.; Matsuda, M.; Tei, K.; Kawai, H. *Macromolecules* **1981**, *14*, 154.
(59) Pak, H.; Flory, P. J. *J. Polym. Sci., Polym. Phys. Ed.* **1979**, *17*, 1845.
(60) Rivlin, R. S.; Saunders, D. W. *Philos. Trans. R. Soc. London* **1951**, *A243*, 251.
(61) Boue, F.; Edwards, S. F.; Vilgis, T. A. *J. Phys. Fr.* **1988**, *49*, 1635.
(62) Vilgis, T. A. *Prog. Colloid Polym. Sci.* **1992**, *90*, 1.
(63) Jones, J. L.; Marques, C. M. *J. Phys. Fr.* **1990**, *51*, 113.
(64) Terentjev, E. M. *Proceedings of the NATO Advanced Research Workshop, Manipulation of Organization in Polymers using Tandem Molecular Interactions*, Pisa, Italy, May 29−June 2, 1996.
(65) Finkelmann, H.; Brand, H. R. *Trends Polym. Sci.* **1994**, *2* (7), 222−226.
(66) Oleinik, E. F. *Adv. Polym. Sci.* **1986**, *80*, 49.
(67) *Materials Science and Technology: A Comprehensive Treatment*; Cahn, R. W., Haasen, P., Kramer, E. J., Eds.; 1993; Vol. 12, Chapter 10, pp 428−467.
(68) Bowden, P. B. *The Physics of Glassy Polymers;* Haward, R. N., Ed.; Wiley: New York, 1973; Chapter 5, pp 279−339.
(69) Kinloch, A. J.; Young, R. J. *Fracture Behavior of Polymers*; Applied Science: New York, 1983; Chapters 4, 5, and 8.
(70) Robertson, R. E. *J. Chem. Phys.* **1966**, *444*, 3950.
(71) Arruda, E. M.; Boyce, M. C. *J. Mech. Phys. Solids* **1993**, *41* (2), 389−412.
(72) Wu, P. D.; Van Der Giessen, E. *J. Mech. Phys. Solids* **1993**, *41* (3), 427−456.
(73) Krupenkin, T. N. Microscopic Model of True Strain Softening and Hardening in a Polymer Glass. Annual Conference of the American Physical Society, Poster Session M29.06, Kansas City, KS, March 20, 1997.
(74) Young, R. J. *Developments in Polymer Fracture-1*; Andrews, E. H., Ed.; Applied Science: London, 1979; Chapter 4.
(75) Cherry, W.; Thomson, K. W. *J. Mater. Sci.* **1981**, *16* (7), 1913−1924.
(76) Berry, J. P. *J. Polym. Sci.* **1961**, *50*, 107.
(77) Gledhill, R. A.; Kinloch, A. J.; Yamini, S.; Young, R. J. *Polymer* **1978**, *19*, 574.
(78) Pritchard G.; Rhoades, G. V. *Mater. Sci. Eng.* **1976**, *26*, 1.
(79) Young, R. J. *Developments in Polymer Fracture-1*; Andrews, E. H., Ed.; Applied Science: London, 1979; Chapter 6.
(80) see for example: *Polymer Toughening*; Arends, C. B., Ed.; Marcell Dekker: New York, Basel, Hong Kong, 1996.
(81) Kiefer, J.; Hilborn, J. G.; Manson, J. A. E.; Leterrier, Y.; Hedrick, J. L. *Macromolecules* **1996**, *29*, 4158−4160.
(82) See for example: Kramer, E. J.; Berger, L. L. *Adv. Polym. Sci.* **1990**, *91/92*, 1−68.
(83) Bucknall, C. *Toughened Thermoplastics*; Wiley: New York, 1977.
(84) Riew, C. K.; Gillham, J. K. *Rubber Modified Thermoset Resins*; Advances in Chemistry 208; American Chemical Society: Washington, DC, 1984.
(85) Riew, C. K. *Rubber Toughened Plastics*; Advances in Chemistry 222; American Chemical Society: Washington, DC, 1989.
(86) Riew, C. K.; Kinloch, A. J. *Toughened Plastics*; Advances in Chemistry 233; American Chemical Society: Washington, DC, 1993.
(87) Shaw, S. J. In *Rubber Toughened Engineering Plastics*; Collyer, A. A., Ed.; Chapman and Hall: London, 1994; Chapter 6.
(88) Bucknall, C. B.; Patridge, I. K. *Polymer* **1983**, *24*, 639.
(89) Diamant, J.; Moulton, R. J. *Natl. Sampe Symp., 29th* **1984**, *29*, 422.
(90) Hedrick, J. L.; Yilgor, I.; Wilkes, G. L.; McGrath, J. E. *Polym. Bull.* **1985**, *13*, 201.
(91) Huang, Y.; Kinloch, A. J. *Polymer* **1992**, *33*, 1330.
(92) Guild, F. J.; Kinloch, A. J. *J. Mater. Sci.* **1995**, *30*, 1689.
(93) It has been shown that oriented polymers exhibit much lower moduli when strained perpendicular to the direction of orientation. (*Structure and Properties of Oriented Polymers*; Ward, I. M., Ed.; Applied Science Publishers: Ltd.: London, 1975; Chapter 7).
(94) Ortiz, C.; Belenky, L.; Ober, C. K.; Kramer, E. J. Submitted for publication, 1997.
(95) Dieter, G. E., Jr. *Mechanical Metallurgy*; McGraw-Hill Book Co., Inc.: New York, Toronto, London, 1961; pp 202−205.

MA971439N